

# Transonic flow field in critical flow Venturi nozzle

T. Kreuzová<sup>a,\*</sup>

<sup>a</sup>Department of Fluid Dynamics and Thermodynamics, Faculty of Mechanical Engineering, Czech Technical University in Prague, Technická 4, 16607, Prague 6, Czech Republic

Received 28 November 2023; accepted 24 May 2024

## Abstract

In this paper, theoretical and numerical analysis of a transonic flow field of critical flow Venturi nozzles according to the ISO 9300 standard is performed. Deviations of the flow field from an estimate based on one dimensionality are clarified. While the theoretical analysis allows prediction of these deviations, the numerical analysis allows quantification of their influence. The main studied phenomena include the local supersonic compression in transonic expansion and the Prandtl-Meyer expansion. The tendency of the flow field to spatial oscillations is shown, alongside the ability of the system to damp these oscillations.

© 2024 University of West Bohemia.

*Keywords:* transonic flow, shock wave, ISO 9300

## 1. Introduction

The ISO 9300 standard [6] is widely used for measuring the mass flow rates of air, natural gas, nitrogen, etc. With recent growth of hydrogen technologies, the usage of this standard to hydrogen flows is desirable and will require its extension. Considering the rather specific properties of the hydrogen (see, e.g., [3]), it is in the interest of high quality measurement to recognize, which phenomena originate in the flow itself (geometry of the nozzle, transonic phenomena, transition to turbulence, etc.) and are, therefore, not only linked to the properties of the real gas.

The ISO 9300 standard allows evaluation of mass flow rate of a gas in a system by using the critical flow Venturi nozzle (CFVN). This is possible due to aerodynamic choking and extensive experimental work that allowed specification of the discharge coefficient ( $C_d$ ) for a wide range of Reynolds numbers related to throat parameters:  $Re \in (2.1 \times 10^4, 3.2 \times 10^7)$  for the toroidal nozzle and  $Re \in (3.5 \times 10^5, 1.1 \times 10^7)$  for the cylindrical nozzle.

The geometry of the nozzles defined by the standard is illustrated in Fig. 1, where the dimensionless radius (shape of the nozzle)  $R^+ = 2R/d^*$  and the distance along the  $x$ -axis  $x^+ = 2x/d^*$  are introduced to simplify comparison. The shape of the cylindrical nozzle is given as

$$R_{\text{cyl}}^+ = \begin{cases} 3 - \sqrt{4 - (x^+ + 2)^2} & \text{for } x^+ \in (-4, -2], \\ 1 & \text{for } x^+ \in (-2, 0], \\ 1 + x^+ \sin(\frac{\alpha}{2}) & \text{for } x^+ > 0, \end{cases} \quad (1)$$

whereas the shape of the toroidal one as

$$R_{\text{tor}}^+ = \begin{cases} 5 - \sqrt{16 - (x^+)^2} & \text{for } x^+ \leq 4 \sin(\frac{\alpha}{2}), \\ 1 + x^+ \sin(\frac{\alpha}{2}) & \text{for } x^+ > 4 \sin(\frac{\alpha}{2}). \end{cases} \quad (2)$$

\*Corresponding author. Tel.: +420 602 102 646, e-mail: Terezie.Kreuzova@fs.cvut.cz.  
<https://doi.org/10.24132/acm.2024.880>

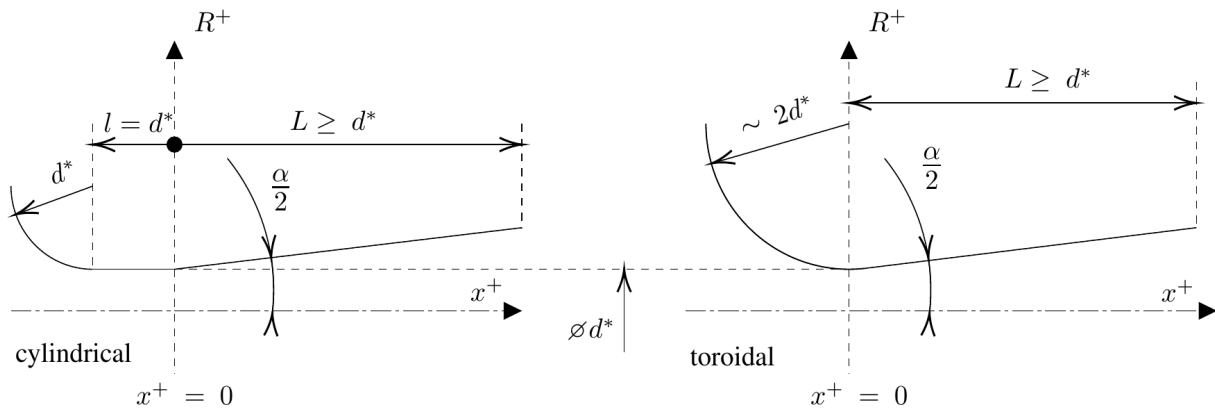


Fig. 1. Types of critical flow Venturi nozzles

The nozzles of cylindrical type consist of quarter of an annuloid, cylinder and a cone. In the toroidal ones, the conical part is directly tangentially connected to a part of an annuloid. The standard allows the angle  $\alpha/2 \in [2.5, 6]^\circ$ . It should be noted that the recommended values of  $\alpha$  for the Laval nozzles are  $\alpha \in [8, 12]^\circ$ .

Under the transonic conditions, the flow is aerodynamically choked and therefore – following the 1D theory – the ideal mass flow rate  $q_{mi}$  equals to the product of the critical speed of sound  $a^*$ , critical density  $\rho^*$  (dependent on stagnation properties denoted by the lower index '0': the stagnation pressure  $p_0$  and the stagnation temperature  $T_0$  in (3), and the properties of the ideal gas, namely: the specific gas constant  $r$  and the ratio of specific heats  $\kappa$ ) and the minimal cross-section of the nozzle  $A^*$ ,

$$q_{mi} = A^* \underbrace{\sqrt{\kappa \left( \frac{2}{\kappa + 1} \right)^{\frac{\kappa + 1}{\kappa - 1}} \frac{p_0}{\sqrt{r T_0}}}}_{a^* \rho^*}. \quad (3)$$

This ideal mass flow rate is corrected by  $C_d = C_d(\text{Re}) < 1$  to obtain the real mass flow rate

$$q_m = C_d q_{mi}. \quad (4)$$

The coefficient  $C_d$  should incorporate influence of higher geometrical dimensionality of the flow and boundary layer properties (especially its displacement thickness). Properties of real gas are not reflected in this work, therefore, its implementation in the standard is not further commented here.

An immense amount of theoretical (e.g., [5]) and experimental (e.g., [13,14,23]) works have been conducted in order to evaluate  $C_d$  more accurately. Yet, some small and rather interesting problems of this – simple at first glance – flow remain open.

In this work, the flow field of the nozzles is analyzed. Single phenomena related to transonic behavior occurring in the nozzles are studied. Following the investigation of the shape and position of the sonic line, local supersonic compression in transonic expansion and in the Prandtl-Meyer expansion are investigated.

For calculations, where the dimensions of the nozzle need to be set exactly, the following values were used:  $d^* = 10 \text{ mm}$ ,  $L = 2d^*$ ,  $\alpha/2 = 6^\circ$ . The highest allowed value of  $\alpha/2$  is selected to show, whether local supersonic compression in transonic expansion can be present in all devices across the possible range of the angle  $\alpha$ . An ideal gas with constant properties of

air is considered, i.e., the specific gas constant  $r = 287.05 \text{ J kg}^{-1} \text{ K}^{-1}$ , the ratio of specific heats  $\kappa = 1.4$ , the dynamic viscosity  $\mu = 1.5 \times 10^{-5} \text{ Pa s}$ , and the Prandtl number  $\text{Pr} = 0.72$ . The total conditions at the inlet of the nozzle are also given. The total pressure  $p_0 = 1 \times 10^5 \text{ Pa}$  and the total temperature  $T_0 = 303.15 \text{ K}$  are assumed. Therefore, the Reynolds number  $\text{Re} = 1.5 \times 10^5$  is reached at the throat of both nozzles (characteristic length is the critical diameter  $d^* = 10 \text{ mm}$ ,  $\rho^* = 0.708 \text{ kg m}^{-3}$ ,  $a^* = 318.626 \text{ m s}^{-1}$ ).

## 2. Numerical analysis

The numerical analysis of the flow is performed to support and enrich theoretical findings. Its results are presented in Section 3. All of them were acquired with the setup described in the following paragraphs. The meshing and the simulation were carried out in the open source CFD software OpenFOAM (v2112). The post-processing was done using the ParaView visualization engine [1].

The numerical simulation of flow in the CFVN with axisymmetric model was performed. Turbulent flow of compressible fluid modeled as an ideal gas (the system is closed by  $p = rT\rho$ ) is considered [4]

$$\begin{aligned} \frac{\partial \rho}{\partial t} + \nabla \cdot (\rho \mathbf{U}) &= 0, \\ \frac{\partial (\rho \mathbf{U})}{\partial t} + \nabla \cdot (\rho \mathbf{U} \otimes \mathbf{U}) &= \nabla \cdot \boldsymbol{\tau}_{eff}, \\ \frac{\partial (\rho E)}{\partial t} + \nabla \cdot [(\rho E + p) \mathbf{U}] &= \nabla \cdot [\boldsymbol{\tau}_{eff} \cdot \mathbf{U}] + \nabla \cdot (\lambda_{eff} \nabla T), \end{aligned} \quad (5)$$

where  $\mathbf{U}$  is the velocity vector,  $\boldsymbol{\tau}_{eff}$  is the effective stress tensor,  $\lambda_{eff}$  is the effective thermal conductivity and  $E$  is the specific total energy ( $E = e + \|\mathbf{U}\|^2/2$ , where  $e$  is the specific internal energy).

The given set of equations (5) is discretized by the finite volume method (FVM). The time discretization is performed by the Euler implicit time scheme. For the solution of the resulting system of algebraic equations, the lower-upper symmetric Gauss-Seidel scheme is used (solver is described in [4]). The steady state of the choked flow is sought.

The Langtry-Menter 4-equation transitional SST turbulence model ( $\gamma\text{-Re}_{\theta t}$ ) [11] was applied as a strong favorable pressure gradient can suppress turbulent fluctuations in the boundary layer and, therefore, decrease its thickness, which is crucial for the evaluation of  $C_d$ . To quantify the possible influence of the mentioned gradient, the coefficient

$$K(x) = \frac{\nu}{U_x(x)^2} \frac{dU_x(x)}{dx} \quad (6)$$

is used, where  $U_x(x)$  is the velocity of the main flow,  $\nu$  is the kinematic viscosity and  $x$  stands for the coordinate along the axis.

If  $K > K_{lim}$ , relaminarization of the boundary layer can be expected. The critical value  $K_{lim}$  of the coefficient  $K$  is a subject of discussion, but there is a general consensus [8,12,15,20] on  $K_{lim} \in [3 \times 10^{-6}, 4 \times 10^{-6}]$ . In this work, we consider  $K_{lim} = 3.6 \times 10^{-6}$ . Development of  $K$  along the nozzles is shown in Fig. 3. More details on this figure are given in Section 3. Damping of turbulent fluctuations can be expected in the whole toroidal part of both nozzle types. Therefore, to allow – as precise as possible – boundary layer thickness computation, a model, which takes intermittency  $\gamma$  into account, needs to be utilized. The equations for  $\gamma$  and

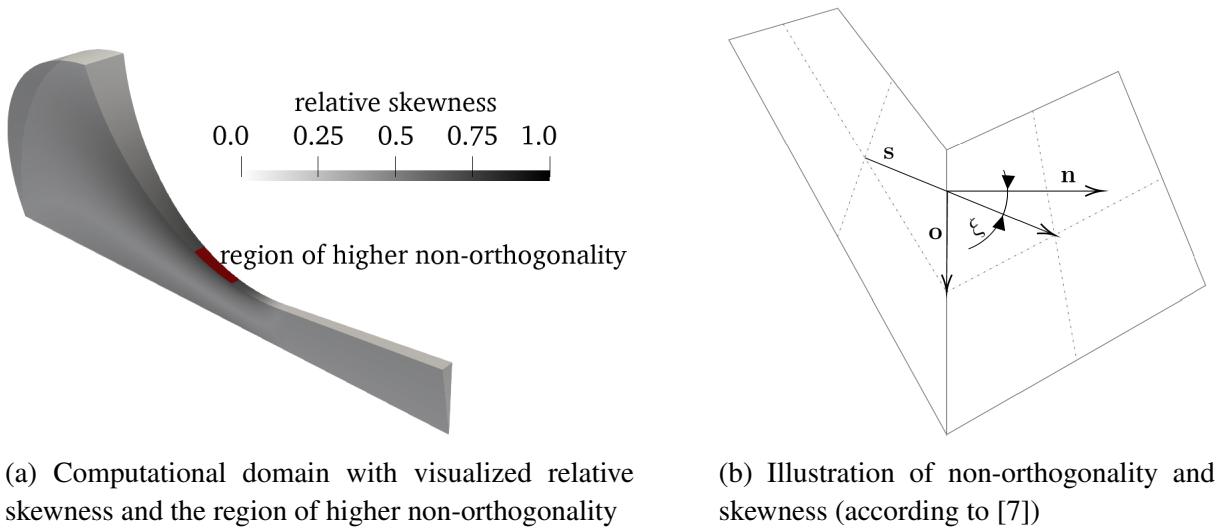


Fig. 2. Illustration of mesh quality properties – orthogonality and skewness

$Re_{\theta t}$ , added to the SST  $k-\omega$  model by [11] to create the  $\gamma-Re_{\theta t}$  model, describe the laminar–turbulent (and reverse) transition process.

When the choked state is reached, the inlet is subsonic, whereas the outlet is supersonic<sup>1</sup>, therefore, for the open boundaries, the total pressure and the total temperature at the inlet are prescribed ( $1 \times 10^5$  Pa and 303.15 K, respectively, as stated in Introduction). Homogeneous Neumann boundary conditions ( $\frac{\partial \cdot}{\partial n} = 0$ ) are prescribed for  $U$ ,  $p$ ,  $T$  at the outlet and for  $U$  at the inlet. At the wall, standard boundary conditions were applied (homogeneous Dirichlet boundary condition for  $U$  and homogeneous Neumann conditions for  $p$ ,  $T$ ). In terms of turbulence modeling, turbulent intensity ( $Tu = 3.3\%$ ), turbulence length scale ( $Tu_L = 4 \times 10^{-3}$  m) and intermittency  $\gamma = 1$  are assumed at the inlet.  $Re_{\theta t}$  is computed according to the requirements of the model. On the pair of patches coincident with the axis in the swirl direction, a cyclic condition assuring axisymmetry of the flow is applied.

The computations were performed on hexahedral meshes with refinement at the wall generated within the blockMesh utility, supplied with OpenFOAM. The refinement ensures that the dimensionless size of the cell at the wall is close to one (i.e.,  $y^+ \approx 1$ ) and the growth in the normal direction to the wall is gradual. The value of  $y^+$  was verified after computation, in all cases computed with a fine grid,  $y^+ < 1.6$ , with a medium grid,  $y^+ < 2.5$ , and with a coarse grid,  $y^+ < 3.9$ . Higher values were obtained only in the region near the inlet.

For the case of the toroidal nozzle, a mesh of the lowest quality (higher skewness and non-orthogonality) is located near the wall at  $x^+ \approx -1$ . This is illustrated in Fig. 2a, in which the relative skewness stands for the ratio of local and maximum skewness in the domain. Similarly, the mesh of the lowest quality in the cylindrical nozzle is located at  $x^+ \approx -3$ . Properties of the meshes are given in Table 1, where  $\frac{\|o\|}{\|s\|}$  stands for the skewness and  $\xi$  for the non-orthogonality. An illustration of the geometric properties is given in Fig. 2b. As the non-orthogonality of a few cells in toroidal nozzle is quite high, non-orthogonal corrections are employed in the computation.

<sup>1</sup>The supersonic outlet is assumed to ensure that the flow is supersonic in the whole diverging part of the nozzle and is not disturbed by any instability connected to a strong shock wave (studied, for example, in [23]) or outlet to a large tank. With such strong phenomena present, small oscillations studied in Section 3 are easily neglected. This leads to the back pressure being a result of a computation and not a boundary condition.

Table 1. Mesh quality metrics

	$\max\left(\frac{\ o\ }{\ s\ }\right)$	$\text{avg}(\xi)[^\circ]$	$\max(\xi)[^\circ]$
cylindrical	0.86	10	47
toroidal	0.32	24	70

A mesh independence study was performed for the toroidal nozzle. Three – fine (index  $f$ ), medium ( $m$ ), and coarse ( $c$ ) – meshes with the refinement factor  $r = 2.0$  in one direction (leading to a quadrupling of the number of cells in the domain) were considered. An asymptotic value of the outlet mass flow rate  $\dot{m}^*$  [kg s<sup>-1</sup>] was obtained by the Richardson extrapolation

$$\dot{m}^* = \dot{m}_f + \frac{\dot{m}_f - \dot{m}_m}{r^q - 1}, \quad (7)$$

where  $q$  is the estimated order of accuracy ( $q = 1.542$ ). For the studied case, the value of  $\dot{m}^* = 0.01811$  was obtained.

Let us introduce the grid convergence index (GCI) as a measure of how far the value obtained with the given grid is from an asymptotic value, see [17],

$$\text{GCI}_m = \frac{F_S}{r^q - 1} \frac{|\dot{m}^* - \dot{m}_m|}{\dot{m}^*}. \quad (8)$$

With the outlet mass flow rate as the target quantity, GCI with the safety factor  $F_S = 3.0$  of the medium grid with 312 500 cells (250 cells in the radial direction) is  $9.633 \times 10^{-4}$ . The mass flow rate computed with the medium mesh differs from the one predicted by the ISO 9300 standard by 0.42 % and with the fine mesh by 3.81 %.<sup>2</sup> These results can be taken as satisfactory.

In selected cases, the simulation of inviscid fluid flow can be beneficial. In those cases, the mesh is not refined in the vicinity of the wall, a turbulence model is not applied and the velocity in the normal direction to the wall is assumed zero (i.e.,  $U_n = 0$ ) at the wall.

### 3. Transonic phenomena

To emphasize the difference between a one dimensional inviscid and a more detailed description, the development of the Mach number (Ma) along the CFVN axis, given by

$$0 = \frac{1}{\text{Ma}(x)} \left[ \frac{\text{Ma}(x)^2(\kappa - 1) + 2}{\kappa + 1} \right]^{\frac{\kappa+1}{2(\kappa-1)}} - \frac{A^*}{A(x)}, \quad (9)$$

is compared with the flow field obtained by FVM in Fig. 3.<sup>3</sup> As all constants in (9) are known,  $\text{Ma}(x)$  can be found for every  $A(x)$ . A non-linear solver, in this work a modification of the Powell's hybrid method implemented in SciPy [22] is used, needs to be employed and, as solutions in transonics are usually ambiguous, reasonable initial guess for each  $x$  has to be given.

In the subsonic region of the cylindrical nozzle (left column of Fig. 3, label 1), the influence of higher dimensionality and viscosity can be clearly seen. In the simplified solution, a sharp

<sup>2</sup>The coefficient  $C_d$  given by the standard has relative uncertainty 0.2 % at the level of confidence of 95 %.

<sup>3</sup>The numbers (labels) 1 – 9 are used to highlight interesting parts of the plots and are referred to throughout the text.

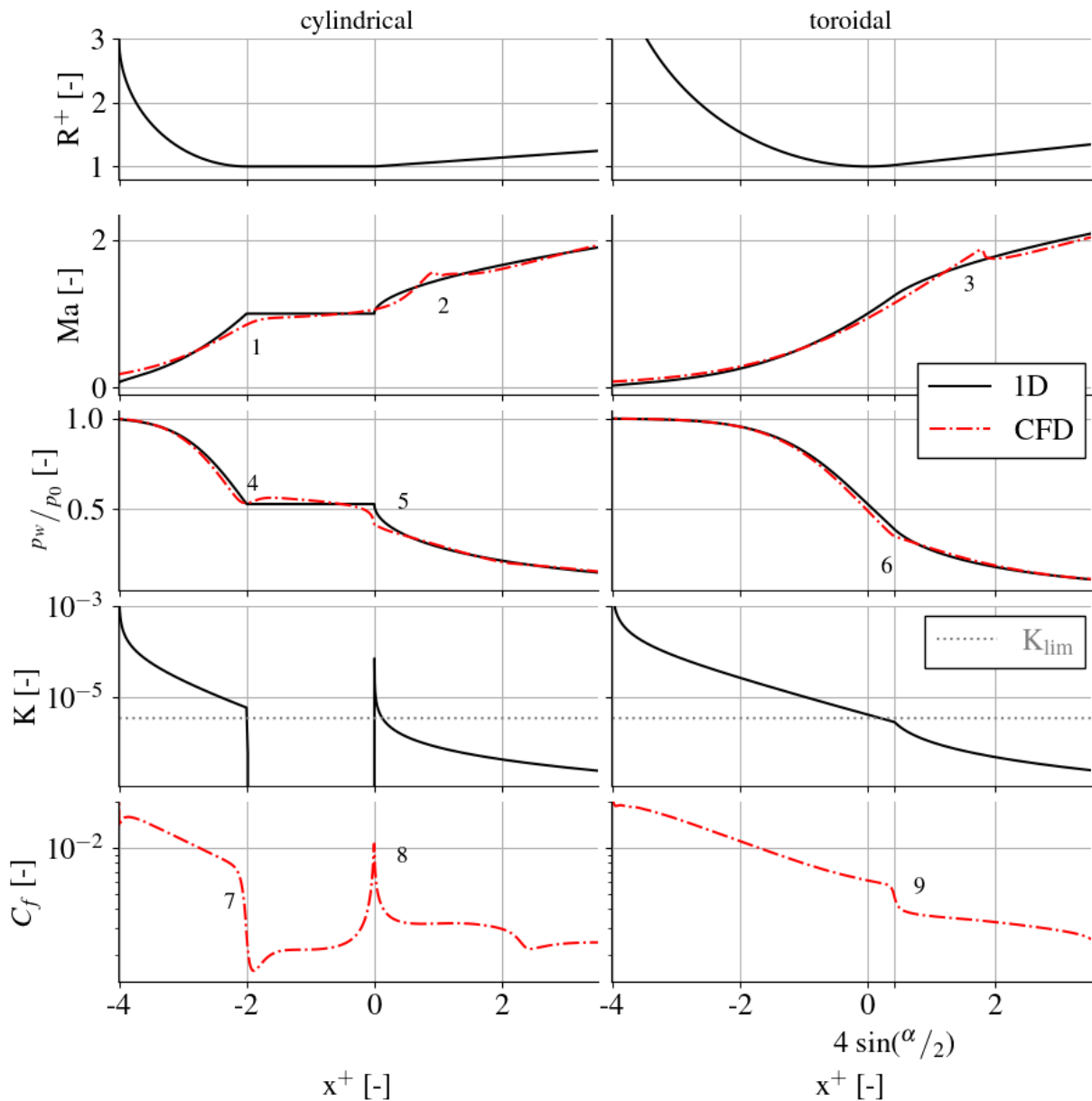


Fig. 3. Development of variables along the CFVN axis

change in the velocity (discontinuity in its first derivation) occurs, but is unnatural and does not correspond to the elliptical character of the equations describing the subsonic flow. This is given by the singularity of the system at  $Ma = 1$ .

The deviations from the 1D solution in the supersonic region are caused by different phenomena. While for the nozzle with the cylindrical throat, the Prandtl-Meyer expansion (Section 3.3) is present – label 2, in the toroidal nozzle, the local supersonic compression in transonic expansion (Section 3.2) – label 3 – is the source of the difference.

### 3.1. Sonic line

The shape of the sonic line is one of the crucial factors for the evaluation of  $C_d$ . The sonic line also splits the solution domain into subsonic and supersonic parts. Thus, it does not only impact  $C_d$ , but also defines where the system describing the (idealized inviscid) flow can be considered

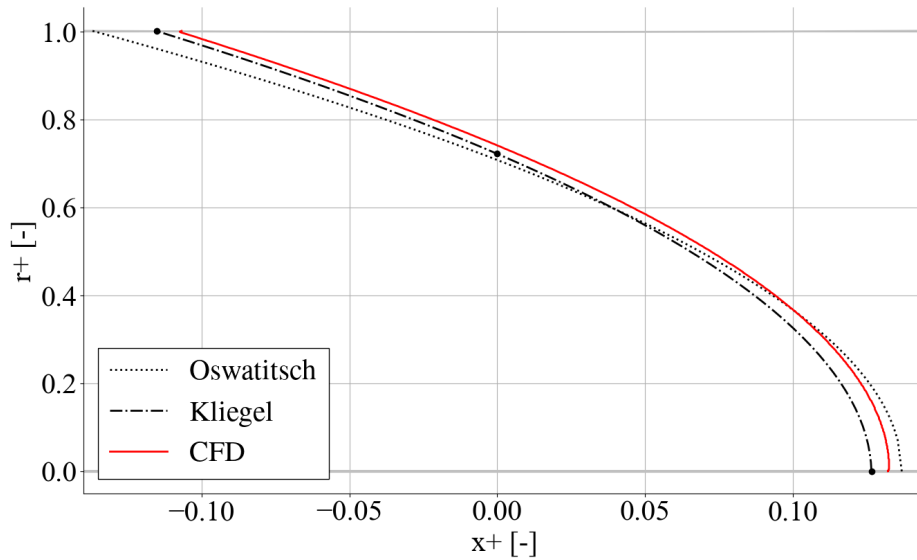


Fig. 4. Sonic line in the toroidal nozzle

hyperbolic and, therefore, suitable for the description by means of the method of characteristics.

For inviscid flow, the approximate shape of the sonic line can be predicted by means of a theoretical analysis. The position of the sonic line lies at the minimum effective cross-section (throat) of the nozzle. The effective cross-section is a cross-section reduced by the displacement thickness of the boundary layer. It should be noted that for viscous flow in the nozzle with a cylindrical throat, the sonic line is shifted near the end of the cylindrical part (visible in the graph of  $Ma(x)$  in Fig. 3). This is caused by the growing boundary layer, which gradually reduces the effective cross-section of the throat. Therefore, a minimum effective cross-section is present near the end of the throat. As a result, the sonic line is not deformed by the wall curvature and is almost straight.

For the toroidal nozzle, the results of the prediction of the sonic line shape, based on the derivation in [9, 16], are to be compared to the shape given by the numerical simulation with inviscid fluid in Fig. 4. The sonic line obtained by Oswatitsch and Rothstein in [16] with geometrical constraints of the toroidal nozzle from the ISO 9300 standard is given by

$$r^+ = \sqrt[4]{\frac{2^5}{\kappa + 1} \left( 5 - \sqrt{2^4 - \frac{\kappa + 1}{2^7}} \right)} \sqrt{\sqrt{\frac{\kappa + 1}{2^7}} - x^+}, \quad (10)$$

where  $r^+$  is the radial coordinate normalized by  $d^*/2$ . In the work [16], a discrepancy between the exact and approximate solutions is shown. Analytically obtained results are compared to experimental data. Apparently, the more the wall is curved the greater error is induced.

The sonic line by Kliegel and Levine [9] is defined by the three points  $[x_{wK}^+, R_{\text{tor}}^+(x_{wK}^+)]$ ,  $[0, r_K^+]$ , and  $[x_{0K}^+, 0]$ , where

$$\begin{aligned} x_{wK}^+ &= \sqrt{\frac{\kappa + 1}{10} \frac{1.14\bar{\kappa}^2 + 8.75\kappa + 44.525}{2280}}, \\ r_K^+ &= \frac{\sqrt{2}}{2} \frac{-1332\kappa^2 + 11613\kappa + 1046097}{1036800}, \\ x_{0K}^+ &= \sqrt{\frac{\kappa + 1}{10} \frac{4440\kappa^2 - 30204\kappa + 520722}{2073600}} \end{aligned} \quad (11)$$

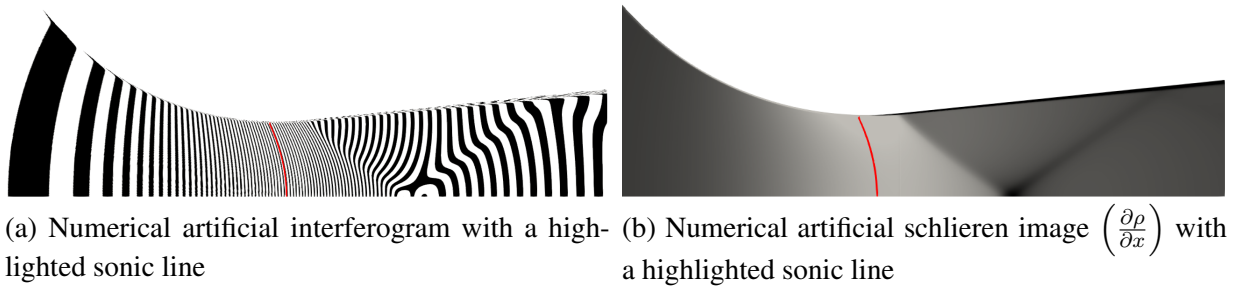


Fig. 5. Flow field in the toroidal nozzle – meridian slice

and  $R_{\text{tor}}^+(\cdot)$  was defined by (2) in Introduction. In Fig. 4, the three points are marked by black dots and a parabolic interpolation between them is shown. As for the previous approximation, the constraints of ISO 9300 are employed.

### 3.2. Local supersonic compression in transonic expansion

A phenomenon originating in an interaction of expansion waves with the sonic line, which – after their reflection – become compression waves, is described and documented in [21]. This interaction is allowed by the geometry of the toroidal nozzle. The connection between the toroidal and conical parts is smooth, but induces a discontinuity in curvature ( $k$  [ $\text{m}^{-1}$ ]). While for  $x^+ < 2d^* \sin(\alpha/2)$ , the curvature is  $k = (2d^*)^{-1}$  [ $\text{m}^{-1}$ ], for  $x^+ > 2d^* \sin(\alpha/2)$ , it is  $k = 0$  [ $\text{m}^{-1}$ ].

A numerical artificial interferogram (with constant  $\Delta\rho = 0.011\,858\text{ kg m}^{-3}$ ) and a schlieren image of meridian slice of a flow field in the toroidal nozzle with weak shock waves caused by Local Supersonic Compression in Transonic Expansion (LSCiTE) are shown in Fig. 5.

In an inviscid flow, LSCiTE could be observed even in the cylindrical type. For the planar case with a constant section of the throat, an analysis to predict the frequency of the LSCiTE is performed in [18]. Its results are adapted for ISO 9300 in [10] and the dimensionless wavelength of the oscillations  $\lambda^+ = 2\lambda/d^*$ , i.e.,

$$\lambda^+ = \sqrt{\frac{\kappa + 1}{2} \frac{12}{13}}, \quad (12)$$

is derived with the assumption that the velocity  $c = a^*$ . For the illustration, see Fig. 6.

The value  $\lambda^+$  in (12) differs from the wavelength predicted by the numerical simulation by about 20%. The discrepancy can be mostly attributed to the difference in the sonic line shape assumed by each method. The derivation in [18] assumes the shape of the sonic line according

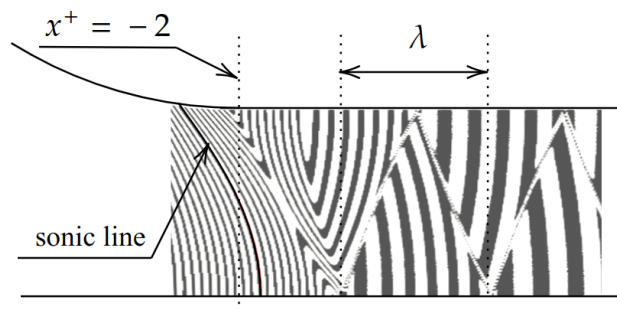


Fig. 6. LSCiTE inviscid planar case with constant throat (section of numerical interferogram) [10]

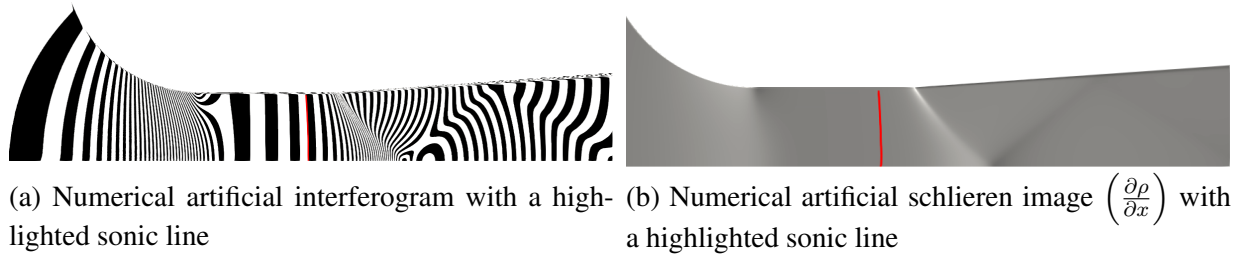


Fig. 7. Flow field in the cylindrical nozzle – meridian slice

to [16]. It is the same method as was used and commented on in Section 3.1. As it has been shown, the shapes do not match perfectly. Also the curvature of the inlet of the cylindrical type is two times higher than in the case of the toroidal nozzle and, therefore, one can expect higher error of the theoretical estimation and also greater difference between the theoretically and numerically obtained values than in the case illustrated in Fig. 4.

In the case of the axisymmetrical nozzle with a toroidal throat, the situation changes. In the region, where LSCiTE is studied, the velocity of the flow increases along the axis and also the reflective boundaries are not parallel. The distance between the interactions of local compression with the wall increases. The positions of the interactions can be predicted by simple trigonometry.

As can be seen in Fig. 3 (toroidal nozzle,  $p_w$ , label 6)<sup>4</sup>, in terms of pressure, the phenomenon is not of great significance in the interaction with the wall. Emphasis should be also placed on the interaction of LSCiTE with the boundary layer. Based on the results of numerical simulations, the turbulence kinetic energy  $k$  is increased in the region of this interaction and a leap in the friction factor  $C_f$ ,

$$C_f(x) = \frac{2\tau_w(x)}{\rho(x)U_x(x)^2}, \quad (13)$$

at the very same region also occurs (Fig. 3, label 9).

In contrast to a 2D planar asymmetrical case, for which (12) was derived, the interaction of compression waves – or more precisely the interaction of the wave with itself – at the axis of the nozzle is present. The amplitude of the local compression is magnified by the interaction and causes quite significant deviation of the Mach number from the idealized assumption (see Fig. 3, label 3).

The diffusive behavior of the flow eliminates the compression and other than first and second interactions with the wall do not seem to have any significance. This holds true even for simulations with long supersonic parts ( $L \geq 5d^*$ ).

### 3.3. Prandtl-Meyer expansion

The Prandtl-Meyer expansion can be observed in the cylindrical type of the nozzle. The Mach number increases from a value only slightly higher than unity (sonic line is positioned near the end of the throat) to a value predicted by the Prandtl-Meyer function. It was recently shown in [2] that this function is valid even for an axisymmetrical case. This value is reached only in the vicinity of the sharp corner, where the expansion can be considered as a local simple wave. As an interaction of characteristics occurs at the axis, this phenomenon becomes more complex and the characteristics of both types are present. This is illustrated by the deformation of interferometric stripes in Fig. 7a behind the expansion fan.

<sup>4</sup>The predicted pressure in Fig. 3 is an isentropic pressure based on the Mach number at the nozzle axis.

In contrast to LSCiTE, the effect of this phenomenon on pressure at the wall is more significant (Fig. 3, label 2). In the simulated case, the decrease of the pressure, shortly after the sonic line, is quite steep. The sharp corner, to which the Prandtl-Meyer expansion is connected, also causes a sudden change in the friction factor  $C_f$  (label 8 in Fig. 3). Again, similarly to LSCiTE, the phenomenon propagates through the nozzle, but is also significantly damped.

#### A short note on the local high subsonic expansion effect in the cylindrical nozzle

A small distortion of the flow field, which cannot be included in transonic phenomena, occurs at the beginning of the throat of the cylindrical nozzle and is noticeable in Fig. 3 (label 4) and Fig. 7. This expansion leads to an increase in the local Mach number nearly up to unity, Fig. 8.

In [16], it was shown that a local increase of the Mach number can be present in converging-diverging nozzles in the subsonic mode. Due to the position of the sonic line near the end of the throat, a situation very similar to the one described in [16] occurs in the cylindrical nozzle. This effect, therefore, does not have to be only related to the discontinuity of curvature of the wall and could be present even, e.g., in a nozzle with hyperbolic (continuously curved) walls.

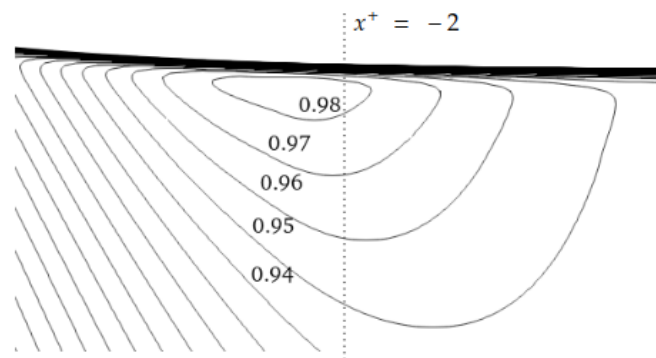


Fig. 8. Iso lines of Mach number – detail of the region near the wall of the cylindrical nozzle at  $x^+ = -2$

#### 4. Conclusions

Flow fields in converging-diverging nozzles according to the ISO 9300 standard were studied both theoretically and numerically. The theoretical relations developed over the second half of the 20<sup>th</sup> century up to the most recent findings are used to identify phenomena occurring in the flow fields. The numerical analysis based on the finite volume method helps to quantify their influence and cover the presence of turbulence.

In the cylindrical nozzle, the first interesting phenomenon is present in the subsonic region, where a local pressure disturbance occurs close to the wall. This can be predicted by the solution of a power series as shown, e.g., in [19]. Theoretically, under suitable conditions, even a small supersonic region can occur in the flow. This local high subsonic effect is definitely worth of a further theoretical study. The subsonic region of the nozzle is closed by a straight sonic line, which is formed near the end of the cylindrical part of the nozzle. The sonic line is followed by the Prandtl-Meyer expansion, which is, close to the sharp corner, formed as a local simple wave, but is instantly deformed by characteristics whose type is changed at the axis. Reflections of emerged waves cause spatial oscillations of the flow, which gradually lose their intensity as they are damped by diffusive behavior of the flow.

In the toroidal nozzle, the subsonic region is closed by a parabolically curved sonic line. The shape of the sonic line can be – with limited precision – estimated analytically. The sonic line is positioned close to a discontinuity of the curvature of the nozzle wall. This discontinuity causes a formation of local supersonic compression in the transonic expansion. Compression waves, which are reflected at the axis similarly to the case of the cylindrical nozzle, cause damped spatial oscillations of the flow field. Wavelength of the oscillations in a simplified case can be also assessed analytically and the difference between this assessment and the numerically obtained values can be justified by differences in the assumptions of these approaches.

While it is evident that nozzles operated under appropriate conditions are not too sensitive to the studied phenomena, these should not be condemned for operation of the nozzles with limit pressure ratio, where they can magnify the instabilities of the flow. Also as the pressure disturbance caused by a local supersonic compression in the transonic expansion can lead to the transition of the originally laminar boundary layer, its presence should not be condemned for detailed numerical studies of the flow fields in nozzles according to ISO 9300 as it can influence the effective cross section of the throat and, therefore, the discharge coefficient, as well.

From the practical point of view, the results presented in this work could be extended to imperfect geometries of real nozzles affected by manufacturing inaccuracies. The influence of a given inaccuracy is driven by its shape and position. As far as pure transonics is concerned, the most interesting imperfections lie in between the sonic point and the point of interaction of the second neutral characteristics with the wall. Changes in geometry before the interaction of the first neutral characteristics with the wall deform the sonic line and are, therefore, able to not negligibly affect the mass flow through the nozzle. Research in the field of these influences would certainly be a beneficial continuation of this work.

## Acknowledgements

The author would like to gratefully thank Professor Pavel Šafařík for his guidance in the field of gas dynamics.

This work was supported by the Grant Agency of the Czech Technical University in Prague, grant No. SGS23/105/OHK2/2T/12. Computational resources were provided by the e-INFRA CZ project (ID:90254), supported by the Ministry of Education, Youth and Sports of the Czech Republic.

## References

- [1] Ahrens, J., Geveci, B., Law, C., ParaView: An end-user tool for large-data visualization, In: Visualization handbook, (eds) C. D. Hansen, C. R. Johnson, Academic Press, 2005, pp. 717–731. <https://doi.org/10.1016/B978-012387582-2/50038-1>
- [2] Chen, K., Xu, J., Qin, Q., Huang, S., Analytical solution of supersonic axisymmetric flow around a sharp convex corner, *Physics of Fluids* 35 (1) (2023) No. 016118. <https://doi.org/10.1063/5.0134698>
- [3] Colonna, G., D’Angola, A., Capitelli, M., Statistical thermodynamic description of H<sub>2</sub> molecules in normal ortho/para mixture, *International Journal of Hydrogen Energy* 37 (12) (2012) 9 656–9 668. <https://doi.org/10.1016/j.ijhydene.2012.03.103>
- [4] Fürst, J., Development of a coupled matrix-free LU-SGS solver for turbulent compressible flows, *Computers & Fluids* 172 (2018) 332–339. <https://doi.org/10.1016/j.compfluid.2018.04.020>
- [5] Ishibashi, M., Takamoto, M., Theoretical discharge coefficient of a critical circular-arc nozzle with laminar boundary layer and its verification by measurements using super-accurate nozzles,

- Flow Measurement and Instrumentation 11 (4) (2000) 305–313.  
[https://doi.org/10.1016/S0955-5986\(00\)00029-7](https://doi.org/10.1016/S0955-5986(00)00029-7)
- [6] ISO 9300:2022, Measurement of gas flow by means of critical flow nozzles, International Organization for Standardization, 2022.
- [7] Jasak, H., Error analysis and estimation for the finite volume method with applications to fluid flows, Ph.D. thesis, Imperial College London, 1996.
- [8] Jones, W. P., Launder, B. E., The prediction of laminarization with a two-equation model of turbulence, *International Journal of Heat and Mass Transfer* 15 (2) (1972) 301–314.  
[https://doi.org/10.1016/0017-9310\(72\)90076-2](https://doi.org/10.1016/0017-9310(72)90076-2)
- [9] Kliegel, J. R., Levine, J. N., Transonic flow in small throat radius of curvature nozzles, *AIAA Journal* 7 (7) (1969) 1375–1378. <https://doi.org/10.2514/3.5355>
- [10] Kreuzová, T., Complex transonic phenomena in critical flow Venturi nozzle, *Proceedings of Computational Mechanics 2023*, Srní, University of West Bohemia, 2023, pp. 97–100.
- [11] Langtry, R. B., Menter, F. R., Correlation-based transition modeling for unstructured parallelized computational fluid dynamics codes, *AIAA Journal* 47 (12) (2009) 2894–2906.  
<https://doi.org/10.2514/1.42362>
- [12] Launder, B. E., Laminarization of the turbulent boundary layer in a severe acceleration, *Journal of Applied Mechanics* 31 (4) (1964) 707–708. <https://doi.org/10.1115/1.3629738>
- [13] Li, C., Cao, P., Zhang, H., Cui, L., Throat diameter influence on the flow characteristics of a critical Venturi sonic nozzle, *Flow Measurement and Instrumentation* 60 (2018) 105–109.  
<https://doi.org/10.1016/j.flowmeasinst.2018.02.012>
- [14] Mickan, B., Kramer, R., Experiences with sonic nozzles used for different gases and wide range of pressure and temperature conditions, *Proceedings of the 7th International Symposium on Fluid Flow Measurement (7th ISFFM)*, Colorado Springs, CEESI, Inc., 2009, pp. 1–14.
- [15] Narasimha, R., Sreenivasan, K. R., Relaminarization in highly accelerated turbulent boundary layers, *Journal of Fluid Mechanics* 61 (3) (1973) 417–447.  
<https://doi.org/10.1017/S0022112073000790>
- [16] Oswatitsch, K., Rothstein, W., Flow pattern in a converging-diverging nozzle, Report NACA-TM-1215, Langley Research Center, 1949.
- [17] Roache, P. J., Perspective: A method for uniform reporting of grid refinement studies, *Journal of Fluids Engineering* 116 (3) (1994) 405–413. <https://doi.org/10.1115/1.2910291>
- [18] Šafařík, P., Theoretical analysis of transonic expansion in blade cascade, Report No. Z-856/83, Institute of Thermomechanics, Czech Academy of Sciences, 1983. (in Czech)
- [19] Shapiro, A. H., *The dynamics and thermodynamics of compressible fluid flow*, John Wiley & Sons, 1953.
- [20] Sreenivasan, K. R., Laminarescent, relaminarizing and retransitional flows, *Acta Mechanica* 44 (1982) 1–48. <https://doi.org/10.1007/BF01190916>
- [21] Štastný, M., Šafařík, P., Experimental analysis data on the transonic flow past a plane turbine cascade, Volume 1: Turbomachinery, American Society of Mechanical Engineers, 1990, pp. 1–8.  
<https://doi.org/10.1115/90-GT-313>
- [22] Virtanen, P., Gommers, R., Oliphant, T. E., et al., SciPy 1.0: Fundamental algorithms for scientific computing in Python, *Nature Methods* 17 (2020) 261–272.  
<https://doi.org/10.1038/s41592-019-0686-2>
- [23] Wright, J. D., Sims, B. W., McKee, R. J., Gillis, K. A., Johnson, A. N., Carter, M. S., Shinder, I. I., Back pressure ratio and the transonic resonance mechanism of low unchoking in critical flow Venturis, *Proceedings of FLOMEKO 2016*, Sydney, 2016, pp. 1–11.